THE UNIVERSITY of EDINBURGH

Edinburgh Research Explorer

Capturing the Development and Interactions of Wakes in Tidal Turbine Arrays Using a Coupled BEM-DES Model

Citation for published version:
Gajardo, D, Escauriaza, C & Ingram, D 2019, 'Capturing the Development and Interactions of Wakes in Tidal Turbine Arrays Using a Coupled BEM-DES Model', *Ocean Engineering*, vol. 181, pp. 71-88. https://doi.org/10.1016/j.oceaneng.2019.03.064

Digital Object Identifier (DOI):
10.1016/j.oceaneng.2019.03.064

Link:
Link to publication record in Edinburgh Research Explorer

Document Version:
Peer reviewed version

Published In:
Ocean Engineering

General rights
Copyright for the publications made accessible via the Edinburgh Research Explorer is retained by the author(s) and / or other copyright owners and it is a condition of accessing these publications that users recognise and abide by the legal requirements associated with these rights.

Take down policy
The University of Edinburgh has made every reasonable effort to ensure that Edinburgh Research Explorer content complies with UK legislation. If you believe that the public display of this file breaches copyright please contact openaccess@ed.ac.uk providing details, and we will remove access to the work immediately and investigate your claim.

OPEN ACCESS

Download date: 25. Apr. 2024

Capturing the Development and Interactions of Wakes in Tidal Turbine Arrays Using a Coupled BEM-DES Model

Daniel Gajardo[a,b], Cristián Escauriaza[a,b,*], David M. Ingram[c]

[a] *Departamento de Ingeniería Hidráulica y Ambiental, Pontificia Universidad Católica de Chile. Av. Vicuña Mackenna 4860, 7820436, Santiago, Chile.*
[b] *Marine Energy Research & Innovation Center (MERIC), Av. Apoquindo 2827, 7550268, Santiago, Chile*
[c] *Institute for Energy Systems, School of Engineering, The University of Edinburgh, Kings Buildings, Mayfield Rd, EH9 3JL, Edinburgh, United Kingdom*

Abstract

As tidal and hydrokinetic energy systems develop, new tools are needed to assess quantitatively the effects of turbines on the environment and to estimate their performance. When installed in an array, turbine wakes interact, increasing the complexity of the flow and changing their performance. Experimental and numerical approaches have been employed to analyze flows with multiple turbines, but it is not yet clear which level of detail is necessary to represent the flow hydrodynamics and the details of the devices. In numerical approaches, questions remain on the selection of turbulence models and turbine representations, since more realistic but computationally expensive methodologies not necessarily produce an improvement on the understanding of these flows. In this investigation we perform simulations of turbine arrays to study the hydrodynamics of wakes and their interactions, comparing with experiments and previous simulations. We propose a methodology that couples detached-eddy simulations (DES) with Blade Element Momentum (BEM), showing that by capturing the dynamically-rich coherent structures of the flow, we improve the description of mean quantities and turbine performance. The results show that

*Corresponding author
Email address: cescauri@ing.puc.cl (Cristián Escauriaza)

for downstream turbines, there is an accelerated wake development, increasing the temporal variability of the bed shear stress, and the power and thrust coefficients.

Keywords: Tidal turbines, Turbulence, Tidal energy, Numerical Models

1. Introduction

Tidal stream energy constitutes one of the most promising alternatives for generating clean and reliable electricity in the years to come. The high predictability of tidal periods and amplitudes make this technology trustworthy and attractive for the renewable energy sector [1, 2, 3]. Among various design approaches for extracting the tidal energy resource, Horizontal Axis Tidal Turbines (HATTs) are the frontrunners, concentrating most of the research and investments [3, 4, 5, 6]. Nevertheless, there are still multiple challenges that policy-makers, researchers and developers must solve before deploying this type of marine hydrokynetic (MHK) devices in large numbers, with a better understanding of the implications of such installations [3, 4, 6, 7].

As stated by Polagye et al. [8], HATTs affect the flows in tidal channels, extracting energy and generating turbulent wakes, which correspond to regions of higher turbulence and velocity deficits downstream. Therefore, the new flow regime after the extraction of energy changes both, its hydrodynamic conditions and the nature of the tidal resource itself [9]. This can have significant environmental consequences such as changes on the tidal range and on the sediment transport regime, affecting also the energy production of devices installed in these new hydrodynamic conditions. Thus, it is crucial to understand how HATTs interact with the incoming flow, the local environment, and with other devices in their surroundings. The latter point is specially relevant since tidal generation will involve multiple devices installed in an array form. To study these interactions it is necessary to assess the hydrodynamics that underlie the operation of HATT arrays over the wide range of length and time scales involved.

Experimental investigations have been carried out to study the development

of wakes past MHK devices, but most of the research has been limited to analyzing a single device. For example, Chamorro et al. [10] performed an experimental analysis of a single scaled turbine. They concluded that power production is highly linked to the turbulent features on the incoming flow, and described a meandering motion in the turbine wake that had only been previously reported on wind turbines. Mycek et al. [11] studied experimentally how different ambient turbulence levels change the turbine operation and wake development, showing how the upcoming turbulence intensity modifies the wake shape, length, and strength, while also changing the turbine performance. Fewer efforts, however, have been made to experimentally study turbine arrays. Mycek et al. [12] extended their previous work [11], and studied two interacting turbines aligned with the flow, concluding that higher turbulence intensity levels can improve the operation of the downstream turbine by accelerating the rate of recovery for the upstream turbine wake. Stallard et al. [13] conducted experiments with up to ten scaled turbines on several array configurations, discussing the effects on the wake of lateral and longitudinal spacing between devices, emphasizing also the importance of array configuration on wake recovery. These experimental studies underscore the effects of wake interactions on the performance and operation of MHK turbines, providing fundamental insights on the wake hydrodynamics in arrays, but they might also be limited by the physical constraints of laboratory conditions and measurement techniques, which requires the complement of computational simulations.

Numerical models contribute to the scientific understanding of physical processes in turbine arrays, by providing detailed three-dimensional (3D) information on the hydrodynamics of MHK devices, momentum transport mechanisms, and interactions with the boundaries. Using experimental data, we can validate the models to be used later in conditions that are more difficult to be tested experimentally, or to evaluate flow variables that cannot be measured directly in the laboratory.

Computational simulations tend to be easier to modify and they can improve the detail at which information is gathered. By using numerical models we can

investigate multiple array configurations, which yield information on the physical characteristics of tidal turbine wakes over a wide range of flow scales. For flows with multiple devices, models typically require simplified representations for the MHK turbines coupled with numerical solvers for the 3D flow past the devices in high-Reynolds number flows. Various combinations of models for turbines and flows have been applied to simulate arrays, with several advantages and limitations depending on the selection of the methodologies used for the turbulence model, and the resolution of the discretizations in space and time.

From the perspective of the turbine representation, models range from simpler actuator disk models (ADMs), to higher complexity approaches like actuator line models (ALMs), or solving the full turbine geometry. The first approach applies a uniform force to the flow, and it is a computationally inexpensive alternative that allows multiple devices simultaneously, but lose the representation of important elements like rotor swirl [14, 15, 16]. The latter ALMs and models that consider the detailed geometry of the device improve the turbine representation, but require considerably more computational resources, due to computationally expensive interpolations to the grid nodes and therefore have not been used for large turbine arrays, even though they can resolve near-field features and unsteady vortical structures generated by the turbine geometry [17, 18, 19, 20, 21, 22, 23].

Blade Element Momentum (BEM) models are a middle ground between the approaches described above. They incorporate rotational components into the flow and use real turbine geometrical data, distributing the forces of turbine blades onto an actuator disk or volume, but they are not capable of representing discrete blade effects like tip vortices in the flow. They have been widely used to represent tidal and wind turbines, showing overall a good representation of wake hydrodynamics [24, 25, 26].

In terms of the flow simulations, statistical approaches for high-Reynolds number turbulent flows use the unsteady Reynolds-Averaged Navier-Stokes (URANS) equations, in which the velocity and pressure fields are decomposed in mean and fluctuating parts. The effects of the fluctuations on the mean flow, or Reynolds

stresses, are typically represented by an eddy viscosity, which is obtained from a separate set of equations. Using the gradient diffusion approach, isotropic URANS models employ low computational resources, and yield robust solutions with good numerical stability [14, 15, 18, 25]. These models, however, can add considerable dissipation, reducing the ability of predicting detailed unsteady features on the flow and solving large-scale coherent structures that dominate wake development in tidal turbine hydrodynamics.

To capture dynamically-rich turbulent coherent structures in the wakes, more advanced but expensive models based on large-eddy simulations (LES) can provide accurate descriptions of these flow fields, yielding detailed solutions by resolving directly all the turbulent scales larger than the size of the computational grid. This produces information on the flow unsteadiness, turbulence, and vortical structures, and therefore it has been used to study tidal turbines, but limited to few devices due to its larger computational cost [16, 17, 18, 19, 22, 23]. To decrease the computational costs required to resolve the turbulent structures of the boundary layer, hybrid URANS-LES models have been proposed (e.g. [27]) that use a URANS turbulence closure near solid walls to allow a coarser grid resolution near the boundaries, while LES is used in the rest of the domain. These models are ideally suited for high-Reynolds number flows past HATT arrays, since they can resolve the most energetic scales of motion away from the walls and the bed, in the turbine wakes.

Taking into account the variety of options to study tidal turbine flows numerically, it is important to consider that the tidal energy sector requires efficient and optimized models that are able to study multiple devices simultaneously, with practical use of computational resources [3, 28]. Moreover, it has been demonstrated that turbulence and large-scale structures dominate the performance of tidal turbines, the evolution of their wakes, and their interaction and effects with the flow in the sites where they are installed [10, 17, 22, 23]. Therefore there is a need for efficient methodologies that can provide both the ability to study multiple devices at the same time, while also reporting information on the unsteadiness of the turbulent flows.

The objective of our work is to contribute to the fundamental understanding of flows past multiple MHK turbine arrays, using numerical simulations with a URANS-LES turbulence model to resolve the coherent structures of the flow. We analyze the dynamics of the wakes by simulating the experiments of Stallard et al. [13] and Thomson et al. [29], comparing our results with the experimental data, and with the URANS simulations of Ingram and Olivieri [30]. We seek to understand the relevance of capturing a more detailed dynamics of tidal turbine wakes in arrays, and study the spatial and temporal evolution of turbine performance, wakes, and the effects on the local flow.

We couple BEM with the detached-eddy simulation approach (DES), a hybrid URANS-LES model that has shown to resolve effectively the dynamics of coherent-structure for a variety of turbulent flows in a wide range of Reynolds numbers [31, 32, 27, 33]. We show that using a detailed turbulence model like DES can provide essential insights into wake development and turbine performance, even if our turbine representation approach is simplified. We also provide extended information on both the mean and the instantaneous behavior of fundamental variables for turbine hydrodynamics, performance, and effects, comparing simulation results with cases that consider a single turbine, and arrays of two staggered rows configurations comprised of seven turbines, and ten turbines of two aligned rows of five turbines each.

To incorporate the effects of ambient turbulence on the development of the wakes, we include an unsteady inlet to our simulations, forcing the DES with a synthetic field that is generated by prescribing a Reynolds stress tensor and selecting time and length scales [34], in which we use a random flow generation (RFG) technique [35].

The paper is organized as follows, in Section 2 we explain the BEM model for the turbines and the DES model for the flow, including their coupling and variables used in the analysis. In Section 3 we present the case study used for validation, together with the parameters used in our numerical application. Later, in Section 4 we show the results obtained with the BEM-DES model to this study case, and we discuss the main findings of our investigation. Finally, in

Section 5 we state the concluding remarks and future work of our investigation.

2. Methodology

To study the hydrodynamic effects of tidal turbine arrays, we couple a DES model with a turbine representation model based on BEM. The advantage of DES is that we can capture the instantaneous flow field and turbulence, while BEM allows to incorporate the effect of multiple HATTs simultaneously. The coupling rationale is based on the work by Creech et al. [36], with a turbine model derived from BEM, which calculates lift and drag forces from tabulated airfoil data, and applies them as momentum sink terms to the incompressible Navier-Stokes equations. The computational solver uses non-staggered and structured grids, with generalized non-orthogonal curvilinear coordinates. Grids have higher resolution near cylindrical regions that represent the turbines as discussed in the following sections. Every turbine is represented by a volume V, which is defined by the coordinates of its origin (x_T, y_T, z_T), its radius R and its cylindrical length L, as shown in Figure 1.

The length L is chosen based on the volume occupied by the turbine tested in the experiments of Stallard et al. [13], and the longitudinal distribution of the forces exerted by the devices is based on the BEM model proposed by Creech et al. [36].

At the beginning of each simulation we find and store the coordinates of every mesh node inside the turbines volume. We also store the radial distance between the node and its respective center, the angle between the node and the turbine center (i.e. azimuthal angle), and the blade twist angle and chord length at the node's radial distance. The detailed description of these variables and their calculation are subsequently explained in Section 2.2. It is important to note that only in the grid nodes within turbine volumes these body forces are calculated and passed into the Navier-Stokes solver.

As shown in Figure 2, for every time-step we obtain the local velocity field at every mesh node inside the turbine volume. If the node is outside the turbine

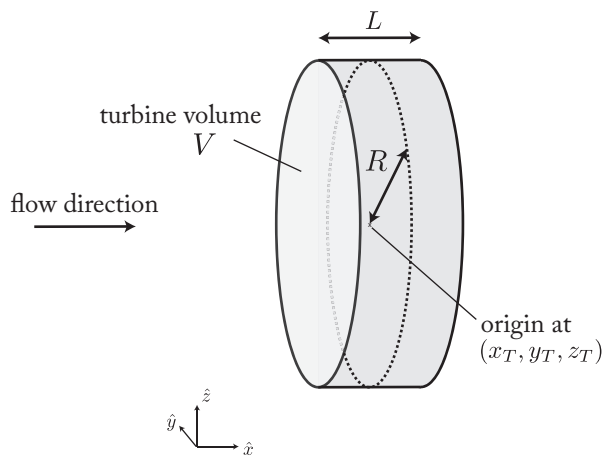

Figure 1: Schematic view of the cylindrical turbine volume V, with radius R and length L. Mesh nodes inside it are used for calculating the body forces that are passed to the Navier-Stokes equations in the DES model.

hub, it calculates nodal lift and drag forces that correspond to body forces in the Navier-Stokes equations, and used to output performance and thrust measurements. If the node is inside the hub region, a zero velocity boundary condition is applied, in order to represent the drag induced on the flow by the structure. This assumption for the hub is a simplified way of considering velocity reduction at turbine hubs without solving their detailed geometry.

2.1. Detached-Eddy Simulation

In our simulations the governing equations are the incompressible, three-dimensional, unsteady, Reynolds-averaged Navier-Stokes equations for the conservation of mass and momentum, solved with the method employed by Escauriaza and Sotiropoulos [32, 37]. In tensor notation, these non-dimensionalized equations can be written as follows,

$$\frac{\partial \tilde{u}_i}{\partial \tilde{x}_i} = 0 \tag{1}$$

$$\frac{\partial \tilde{u}_i}{\partial \tilde{t}} + \tilde{u}_j \frac{\partial \tilde{u}_i}{\partial \tilde{x}_j} = -\frac{\partial \tilde{p}}{\partial \tilde{x}_i} + \frac{1}{Re} \frac{\partial^2 \tilde{u}_j}{\partial \tilde{x}_j \partial \tilde{x}_j} - \frac{\partial}{\partial \tilde{x}_j} \left\langle \tilde{u}_i' \tilde{u}_j' \right\rangle + \tilde{S}_i \tag{2}$$

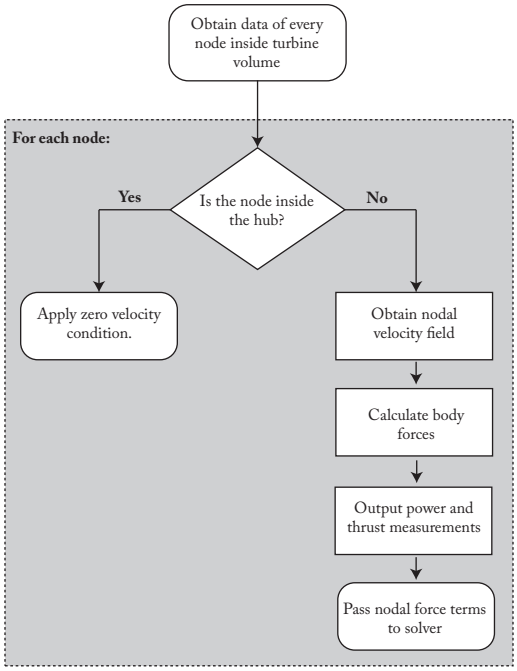

Figure 2: Overview of every time-step calculation procedure.

where $\tilde{S}_i$ is the momentum source (or sink) term, which is only considered in the nodes inside the turbine volumes. The length and velocity scales used for the nondimensionalization of the equations are the mean water depth $\mathcal{H}$ and mean freestream velocity $\mathcal{U}$, respectively.

Here we highlight the main features of the model, and the reader is referred to our previous work for a detailed description of the applications for a variety of turbulent flows in a wide range of Reynolds numbers, as the model has been capable of resolving complex flows dominated by the dynamics of large-scale coherent-structures (e.g. [33, 32, 37]). The DES model is a hybrid formulation that combines URANS and LES, first proposed by Spalart et al. [31] and then revised in [27], which employs the one-equation eddy-viscosity model developed by Spalart and Allmaras [38].

In the DES approach, the turbulence model equation becomes a SGS eddy-viscosity model outside the boundary layer. When the production balances the

destruction term of the model, the length scale in the LES region of the domain yields a Smagorinsky eddy-viscosity. Analogous to the classical LES formulation, the role of this turbulent viscosity is to allow the energy cascade down to a length scale proportional to the grid size, making a pseudo-Kolmogorov length-scale based on the eddy viscosity proportional to the local size of the discretization. As a consequence, when we decrease the grid size the simulations resolve an increasing part of the spectrum, and they do not converge to a grid independent solution.

This model has been extensively tested and validated in previous studies, simulating successfully turbulent flows in complex geometries at high Reynolds numbers. In all these previous studies, the accuracy of the numerical method has been demonstrated by qualitative and quantitative comparisons with available experimental data, in terms of mean flow quantities and turbulence statistics. For these cases, and with similar Reynolds numbers and grid resolutions we resolve up to 90% of the turbulent kinetic energy (see [39, 33, 32, 37, 40], for details).

2.2. Blade Element Momentum

The underlying concepts that explain the motion of HATTs are similar to the ones of airplane wings. Pressure differences between both sides of an hydrofoil generate forces that act on the surface of the hydrofoil and on the fluid moving around it. It is practical to decompose these forces into two components - Lift and Drag - as shown in Figure 3b. Lift force (F_L) acts perpendicular to the velocity faced by the hydrofoil, whereas Drag (F_D) acts on the same direction as the velocity.

To incorporate blade effects onto the fluid we used a model based in a BEM application developed by Creech et al. [36]. Following the approach mentioned there, lift and drag forces per span unit length on the blades can be described

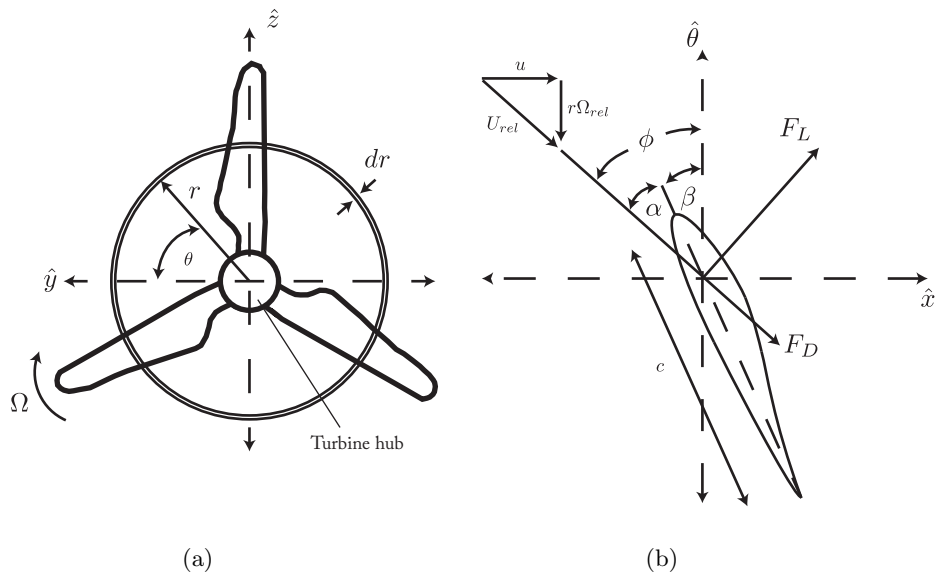

Figure 3: Schematic representation of Blade Element Momentum Theory elements. (a) Frontal view of the blade discretization variables. (b) Variables involved in the lift and drag decomposition in a blade section.

as follows,

$$f_L = \frac{1}{2}\rho\ c(r)\ U_{rel}^2\ C_L\left(\alpha, Re\right) \tag{3}$$

$$f_D = \frac{1}{2}\rho\ c(r)\ U_{rel}^2\ C_D\left(\alpha, Re\right) \tag{4}$$

where ρ is fluid density, U_{rel} is the relative speed between the blades and the fluid and $c(r)$ is the chord length of the blade at a radial distance r from the rotor center. The variables C_L and C_D are the coefficients of Lift and Drag, respectively, which are functions of the airfoil geometry, the angle of attack α, and the Reynolds number Re of the flow over the blade. In order to use these coefficients we use tabulated data that contains their value for different angles of attack and Reynolds numbers. The local velocity field is obtained from the instantaneous numerical solution of the incompressible Navier-Stokes equations. At every time step, we average each component of the velocity within the volume and compute the forces of the BEM as shown in equations 3 and 4.

For a mesh node inside V, and located at a radial distance r from the disk center, relative speed U_{rel} is calculated as:

$$U_{rel} = \sqrt{u^2 + (r\Omega_{rel})^2} \tag{5}$$

where u is the local instantaneous longitudinal velocity component and Ω_{rel} is the relative rotational speed between the blade and the fluid. The latter is written as:

$$\Omega_{rel} = r\Omega + v\sin(\theta) - w\cos(\theta) \tag{6}$$

where θ is the azimuthal angle between the mesh node and the horizontal plane as shown in Figure 3a, v and w are the local transverse and vertical velocity components, respectively, and Ω is the turbine rotational speed. This approach implies that both the rotation of the blades and the fluid are being considered in the calculations. For our application, turbine rotational velocity was considered to be fixed and a function of the turbine tip speed ratio, $\lambda = R\Omega/U_\infty$. The relative flow angle ϕ, shown in Figure 3b, can be obtained as:

$$\phi = \tan^{-1}\left(\frac{u}{r\Omega_{rel}}\right) \tag{7}$$

With this, the local angle of attack is given by the following expression:

$$\alpha(r) = \phi - \beta(r) \tag{8}$$

where β is the local twist angle, defined as the angle variation of the blade from its position at the blade root. This angle is a function of r and depends on turbine blade design. Our model does not consider a dynamic blade pitch control, therefore β remains constant at every radial distance during the simulations.

To incorporate forces per unit length in the Navier-Stokes equations, they must be transformed into body forces (forces per unit of volume), Creech et al. [36] propose using the following expressions,

$$F_L = \eta\left(x^*\right)\left(\frac{N_{blades}}{2\pi r}\right) f_L \tag{9}$$

$$F_D = \eta\left(x^*\right)\left(\frac{N_{blades}}{2\pi r}\right) f_D \tag{10}$$

where N_{blades} is the number of blades and $\eta\left(x^*\right)$ is a Gaussian regularization function used to distribute the forces axially inside the turbine volumes. This regularization function smears out the influence of the blades only axially, since the azimuthal spreading of the forces is handled by the BEM approach with the second term in the equations above. Following Creech et al. [36], the function $\eta\left(x^*\right)$ depends on the longitudinal distance between the mesh node and the disk center, $x^* = x - x_T$, and it is defined as follows,

$$\eta\left(x^*\right) = \frac{1}{\sqrt{2\pi\sigma^2}}\, e^{-\frac{1}{2}\left(\frac{x^*}{\sigma}\right)^2} \tag{11}$$

where the standard deviation σ controls the width of the Gaussian filter. It has been shown that a value of $\sigma = \frac{1}{2}L$, where L is the length of the turbine volume, gives accurate predictions of the turbine performance while controlling the need for excessively high grid resolutions inside the turbine volumes [36].

Lift and drag forces are then decomposed into axial and azimuthal components acting on the fluid. Following Newton's third law, this forces are in the opposite direction to the forces acting on the blade.

$$F_x = -\left(F_L\cos(\phi) + F_D\sin(\phi)\right) \tag{12}$$

$$F_{azim} = -\left(F_L\sin(\phi) - F_D\cos(\phi)\right) \tag{13}$$

The azimuthal component is then written in terms of its lateral and vertical directions

$$F_y = -\sin(\theta)F_{azim} \tag{14}$$

$$F_z = \cos(\theta)F_{azim} \tag{15}$$

Finally, the cartesian components of these forces are non-dimensionalized and incorporated in the governing equations of the flow, where they are applied as source terms within the incompressible 3D momentum equations on each ADMs representing MHK devices.

Since BEM only deals with the section of the turbine that is swept by the blades, when using actuator disks one must decide what to do in the turbine

hub region, the nacelle and the support structure. In our model neither the nacelle nor the support structure were considered. Regarding the hub region, one option is not to apply any body forces in the area, but this has shown to make the hub zone act as a duct, accelerating the flow in it, and therefore negatively affecting overall turbine representation [22]. Another approach is to consider the hub geometry as a solid and build a mesh around it, as it was done in [25, 26, 41, 42]. This gives better representation of the downstream wake but increases meshing complexity and needs an accurate depiction of turbine hub geometry. For our study, since we aim to study large turbine arrays we use a simplified approach to have velocity reduction in the hub, without the need to represent every turbine hub geometry, by applying a zero velocity condition on the grid nodes whose radial distance r is smaller than the radius of the hub. It is important to ponder this simplification when analyzing the results, but as we show in Section 3, it gives good results for wake development when comparing with experimental data and with the overall results of RANS simulations.

2.3. Unsteady inlet

The presence of ambient turbulence can alter wake development and device performance, since fluctuations in the velocity field alter wake momentum exchange processes and local lift and drag characteristics in turbine blades. Previous investigations [19], [16] and [43] have demonstrated these effects of inflow turbulence on HATTs, and stressed the need to consider this issue when modeling devices and studying wake hydrodynamics.

As discussed by Tabor and Baba-Ahmadi [44], there are multiple ways of incorporating inlet conditions in these numerical simulations, which are generally collected into two categories: precursor simulation methods and synthesized turbulence methods. Precursor simulations basically consist of performing a separated detailed LES to generate a database of inlet conditions that can be introduced into the main computation. Even though this approach produces realistic turbulence, it can involve storing large amounts of data and is unwieldy to modify in order to match desired characteristics. Synthesized methods, on

the other hand, are based on producing inlet information from stochastic formulations constrained to desired variables that can be easily modified, which is the main reason why we have chosen them to generate an unsteady inlet in our investigation.

In this case we force the DES with a synthetic field, using a Random Flow Generation (RFG) [35], for which we prescribe a Reynolds stress tensor based on the experimental data, and selecting time and length scales for the incoming flow [34]. The RFG method produces an unsteady turbulent inflow that satisfies the continuity conditions and approximates correctly the anisotropy of the fluctuating field, while being simple to modify in different scenarios. Using a fully-developed URANS mean flow profile as a starting point for the inlet profile, we apply RFG to obtain an inflow boundary condition that respects the previously defined Reynolds stresses (i.e. velocity fluctuation correlations), and the length and time scales of the fluctuations that we wish to simulate.

2.4. Analysis of the flow field

2.4.1. Velocity field

To illustrate longitudinal momentum extraction we use the mean streamwise component of velocity $\langle u \rangle$, and mean velocity deficit U_{def}. The latter is defined as

$$U_{def} = 1 - \frac{\langle u \rangle}{U_{hub}} \tag{16}$$

where U_{hub} is the mean velocity at the inlet and at hub height.

To study the rotational characteristics of turbine wakes we use the mean transverse and vertical components of velocity, $\langle v \rangle$ and $\langle w \rangle$ respectively. Also, we analyze mean axial vorticity $\langle \omega_x \rangle$, defined as:

$$\langle \omega_x \rangle = \frac{\partial \langle w \rangle}{\partial y} - \frac{\partial \langle v \rangle}{\partial z} \tag{17}$$

2.4.2. Turbulence statistics

For analyzing turbulence features we use Turbulent Kinetic Energy (TKE), k, defined as the mean kinetic energy contained in the turbulent velocity fluctuations u', v' and w':

$$k = \frac{1}{2}\left(\langle u'^2 \rangle + \langle v'^2 \rangle + \langle w'^2 \rangle\right) \tag{18}$$

It is also of interest to study Reynolds shear stresses $\langle u_i' u_j' \rangle$, the off-diagonal components of the Reynolds stress tensor. Zones in which these stresses are considerable are regions of increased turbulent mixing, characterized by high velocity gradients and where the effects of turbulent fluctuations on the mean flow increases.

2.4.3. 3D coherent structures visualization

Large-scale unsteady vortices are visualized by using the q-criterion, first proposed by Hunt et al. [45]. Following their definition, coherent structures are identified in the region where

$$q = \frac{1}{2}\left(||\bar{\Omega}||^2 - ||\bar{S}||^2\right) > 0 \tag{19}$$

where $||\bar{\Omega}||$ corresponds to the norm of the rate of rotation tensor, and $||\bar{S}||$ is the norm of the rate-of-strain tensor, both derived from the resolved velocity gradient tensor. This implies that vortices are defined as areas of the flow where the vorticity magnitude is greater than the rate-of-strain magnitude.

2.4.4. Bed shear stress

As discussed in previous investigations [46, 47], HATTs interact with the bed and alter sediment erosion and deposition processes. A way of evaluating these effects is through the shear velocity, which is a parametrization of the shear stress at the bed, and is defined as:

$$u_* = \sqrt{\frac{\tau_0}{\rho}} \tag{20}$$

where τ_0 is the bed shear stress. From our simulations we obtain instantaneous snapshots of u_* and also time averaged values, allowing us to analyze the variability of u_* and possible zones of induced erosion or deposition of sediment due to the presence of HATTs.

2.4.5. Power and thrust coefficients

To analyze turbine dynamics it is common to use the power coefficient C_P and thrust coefficient C_T as indicators for comparison between devices. The power coefficient is defined as the ratio between the power extracted by the turbine blades and the maximum theoretical available power in the incoming flow. We use the following representation:

$$C_P = \frac{P}{0.5\rho U_\infty^3 A_d} \tag{21}$$

where A_d is the frontal area swept by the blades, U_∞ is the freestream velocity upstream of the devices, and power P is obtained by integrating the contribution of every node inside the turbine volume:

$$P = \int_V \Omega \left(r F_{azim} \right) dV \tag{22}$$

The thrust coefficient is defined as the ratio between the axial force acting upon the turbine and the kinetic energy in the incoming flow. We represent this parameter as:

$$C_T = \frac{T}{0.5\rho U_\infty^2 A_d} \tag{23}$$

where the total thrust on the turbine, T, is obtained similarly to P, with:

$$T = \int_V F_x dV \tag{24}$$

3. The PerAWaT case study.

In this study we use our BEM-DES model to compare our simulations with some of the turbine arrays analyzed as part of the Performance of Arrays of Wave and Tidal (PerAWaT) project, commissioned by the Energy Technologies

Institute (ETI) [1]. This is carried out by contrasting our results with the experimental work done by Stallard et al. [13] and Thomson et al. [29], and with the numerical simulations based on the experiments done by Ingram & Olivieri [30]. They used a BEM-URANS model and considered both the turbine nacelle and hub geometry.

3.1. Flume and turbine geometry

Experimental tests were carried out in the University of Manchester wide flume, which has a width of 5 m and a test section 12 m long. The tests were performed with a characteristic water depth of 0.45 m and a mean freestream velocity of 0.45 m/s, which results in a flume Reynolds number of $202,500$. The inlet has a porous weir to produce ambient turbulence intensity of approximately 10% [13]. In the computational domain a rectangular mesh was used to represent the full width and height of the flume. In the streamwise direction the mesh extends $5D$ upstream from the first row of devices and $30D$ downstream from it. Details about the used meshes will be presented in Section 3.3.

In every array configuration identical rotors were used. Each of them has three blades with a Göettingen 804 foil geometry and radial chord length and twist variation. Blades were designed to give similar thrust coefficient variation with tip speed ratio in comparison with a generic full-scale turbine [13]. Key turbine parameters are summarized in Table 1. Because of the increase of meshing complexity and computational cost it would imply, neither the nacelle nor its support structure were considered in our computational simulations.

3.2. Arrays studied

We compare three array configurations studied in [13]. Our starting point is the single turbine array, then we analyze a seven turbine array comprised of two staggered rows separated by 4 diameters (1.08 m), and finally we model a ten turbine array with two aligned rows of five turbines each with 8 diameters of

[1] For more information visit `http://www.eti.co.uk/programmes/marine/perawat`

Table 1: Principal turbine parameters for the studied test case [13].

Symbol	Definition	Value	Unit
D	Turbine diameter	0.27	m
D_h	Hub Diameter	0.03	m
N_b	Number of blades	3	–
U_∞	Mean freestream velocity	0.45	ms^{-1}
Ω	Turbine rotational velocity	15	s^{-1}
λ	Tip speed ratio	4.5	–

longitudinal separation (2.16 m). In every case, the central turbine of the first row is located at the center of the flume, vertically (with the center at a depth of 0.225 m) and laterally. The layouts of the arrays tested in our simulations are illustrated in Figure 4.

In the simulations presented in this work we model the entire channel, including the sidewalls, even though the blockage ratio is 2.54% for a single turbine. For the cases with ten devices, the staggered array has 10.18%, while the blockage for the aligned array is 12.72%.

3.3. Computational grids

Rectangular domains are used for all simulations. In each one of them the number of nodes, the spacing in the near-rotor region of every turbine volume, and the turbine volume cylindrical length were the same, with the values shown in Table 2. Mesh resolution increases near the location of the turbine BEM volumes, as illustrated in Figure 5 for the single turbine case. In the longitudinal direction every turbine volume has five node slices, but vertically and laterally the number of nodes changes because of different mesh stretching conditions at different array configurations. The maximum and minimum number of nodes inside every volume is presented in Table 3. The resolution implemented in our computational grids is sufficient for capturing all the fundamental physical phenomena associated with tidal turbines, with grids that have greater refinement

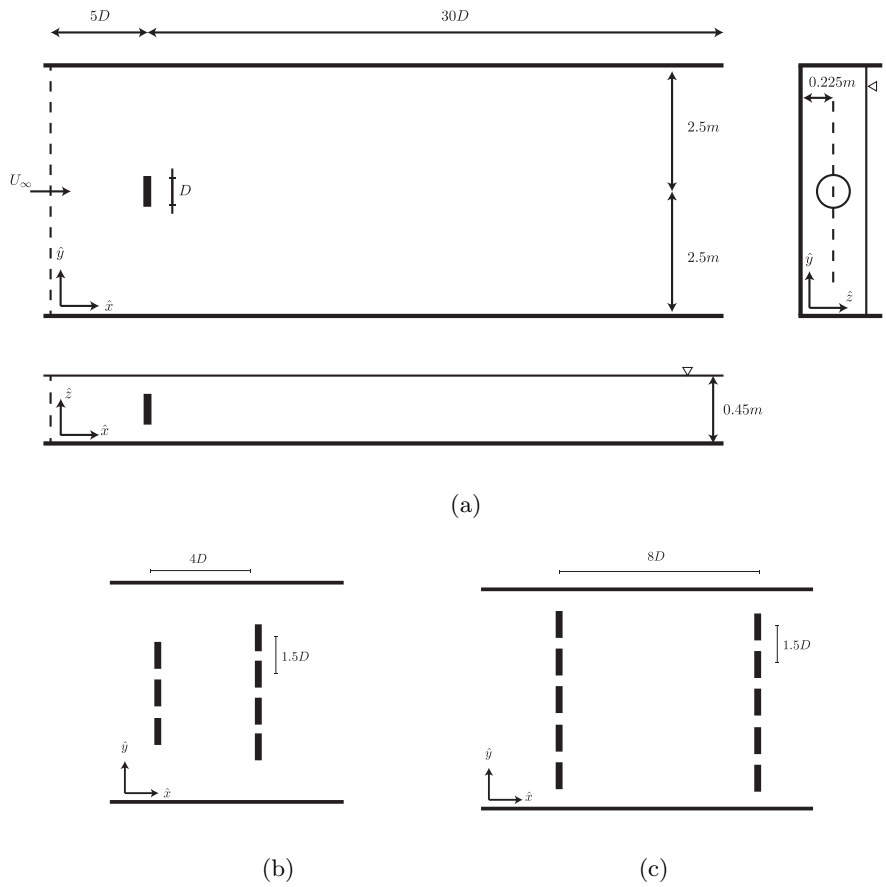

Figure 4: Schematic representation of (a) single turbine case; (b) two staggered rows array and (c) two aligned rows array. Like in the single turbine case, the central turbine of the first row in (b) and (c) is located at the vertical and lateral center of the flume, and at a distance of $5D$ downstream from the inlet. Lateral spacing between devices is the same in every array. The figures are not to scale, so devices seem much closer to flume walls than in the actual experiments, where turbines are far from them and can be considered to be operating without the influence of the flume's lateral boundaries.

than reported models that require more complexity, like the ALMs and solved geometry approaches done by Kang et al. [22] and Chawdhary et al. [23]. This is supported with the results obtained in the simulations, which are reported in Section 4.

Table 2: Details of the parameters used for the computational meshes. N_i and Δi indicate the number of nodes and spacing in the i direction, respectively. (L/D) represents the cylindrical length of the turbine volumes with respect to turbine diameter.

$N_x \times N_y \times N_z$	$282 \times 361 \times 101$
Number of nodes	$10,282,002$
Near-rotor $\Delta x/D$	10^{-2}
Near-rotor $\Delta y/D$	8.3×10^{-3}
Near-rotor $\Delta z/D$	8.3×10^{-3}
Turbine volume (L/D)	4%

Table 3: Minimum and maximum number of nodes inside the turbine volumes for every studied array.

Array	Min. number of nodes inside turbine volume	Max. number of nodes inside turbine volume
Single turbine	$14,560$	–
Two staggered rows	$8,355$	$9,155$
Two aligned rows	$6,865$	$9,230$

3.4. Boundary conditions

All the cases presented in this study have an inlet boundary condition that uses an unsteady flow generator to represent the ambient turbulence in the channel, as reported in the experiments [13, 29]. At the outflow boundary, a zero gradient boundary condition is applied. At the bed of the flume we implement a no-slip boundary condition, with a grid resolution fine enough to resolve the viscous sub-layer in this region. In the lateral walls of the flume,

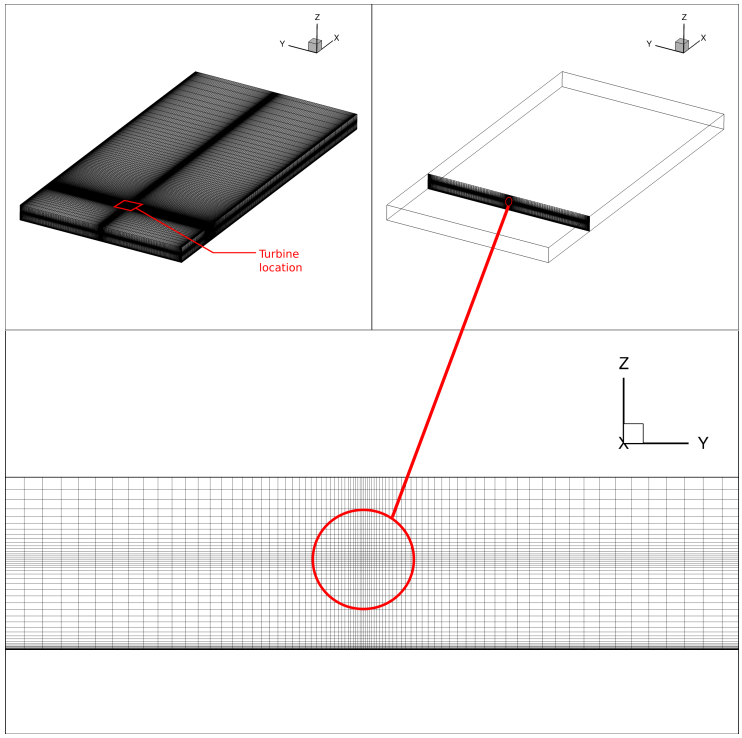

Figure 5: Grid used for the single turbine case, showing in detail the resolution at the device location.

we use wall functions [48] in order to decrease the number of nodes needed in that zone. Finally, even though free-surface effects have been shown to influence tidal turbine operation and wake development [46, 49], it is beyond the scope of this study to incorporate them, and consequently a flat and rigid slip wall with a symmetry boundary condition is used in the top surface of the domain.

4. Results and discussion

In this section we first present and discuss the results for the single turbine case. Thereafter, we present the results obtained for the staggered and aligned rows cases, comparing and contrasting the obtained flow fields, wake structures and performance measurements. To analyze the mean flow we average in time the instantaneous flow field for the equivalent to 450 turbine revolutions in the single turbine case, and for 200 device revolutions for both double row arrays. Since the rotational velocity is equal to 15 rad/s, they correspond to 188.5 s and 83.8 s, respectively. This allows us to capture rich hydrodynamics features of fully developed tidal turbine wakes. We first perform a warming-up period of the simulations, making sure that first and second-order statistics converge before we start collecting the velocity and pressure time series for the analysis. Therefore, the numerical results at $t = 0$ consider a flow that has already converged developed wakes that have interacted with the turbines. Unfortunately not always both numerical and experimental information were available for comparison, but when possible the analysis is made by using both sets of data.

4.1. Single turbine

4.1.1. Mean flow field

We compare the velocity deficit distribution U_{def} with the experimental results for the case of a single turbine. In the near field, the model results exhibit significant differences on the velocity deficit of the wake. The hub modeling approach we employ in the simulations cannot resolve the velocity deficit profile

compared to the experimental data on the near wake region, directly downstream of the nacelle.

These near wake differences are illustrated in Figure 6a, and they are characteristic of BEM approaches which are known to be unable to reproduce correctly the near wake effects [50, 51]. Our simplification of not considering the turbine nacelle and support structure geometry also contribute to this disagreement in the near wake region. The difference diminishes downstream of the turbine, and in the far wake the agreement with experimental observations improves. The axial velocity profile shown in Figure 6b demonstrates this improvement, but still indicates that the simulated velocity distribution along the hub axis tends to be underestimated in the order of 10%, with a similar rate of recovery than the experimental results. This is indicated by the same slope of both curves in the far wake region.

To further look into wake characteristics after a single device we plot in Figure 7 contour plots of mean flow variables for the entire water column. In the simulations, the turbine hub is located at $z = 0.225$ m or $z/D = 0.83$. The lowest point of the turbine blade is located at $z = 0.09$ m or $z/D = 0.33$. The mean longitudinal velocity $\langle u \rangle$ plot indicates momentum extraction and velocity reduction downstream of the turbine, followed by a gradual recovery that lasts up to $20D$ downstream from it. Velocity reduction near the hub produces a reversed flow region immediately downstream from it. The mean transverse velocity $\langle v \rangle$ plot shows an internal zone where the wake rotates in the opposite direction to the turbine blades, and a region downstream of the hub with the same direction of rotation than the blades. These two counter-rotating regions can be better appreciated when plotting axial vorticity $\langle \omega_x \rangle$. Both Figures 7b and 7c show that the produced rotating zones remain mainly columnar up to $5D$, after which rotation decreases and the wake expands radially. These Figures also indicate that BEM is able to reproduce rotational characteristics downstream of the blade region and that our hub approach generates a counter rotating vortex, but that our simulation is still not able to reproduce tip vortices, described in detail in the work done by Kang et al. [22]. These vortices are produced by

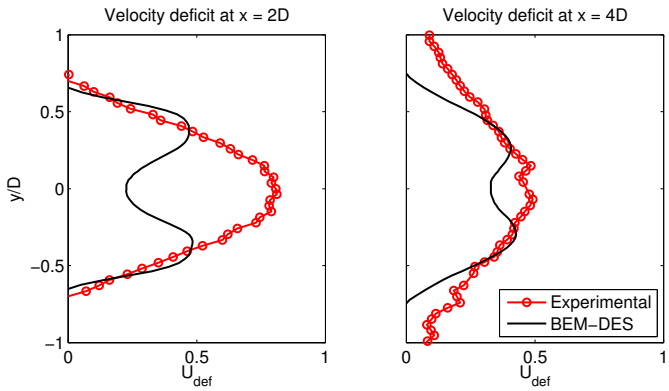

(a)

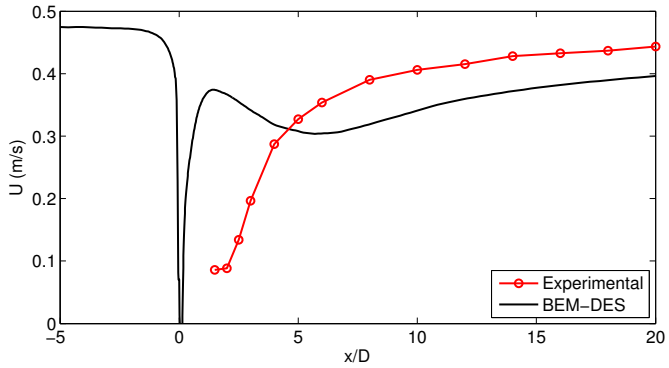

(b)

Figure 6: Lateral and longitudinal plots of axial velocity. (a) Lateral profiles of velocity deficit for the single turbine case. The difference between the curves is explained because of the limitations of BEM applications and our simplification of not simulating the complete hub, nacelle and support structure geometry; (b) Axial velocity profile along the hub axis for a single turbine. Velocity tends to be underestimated in approximately 10% by the BEM-DES model, but both curves show the same rate of recovery.

local effects of turbine tips over the flow that are lost when the turbine effects are smeared over a disk, like in BEM.

When analyzing turbulence statistics depicted in Figure 8 it can be seen that there are two regions where turbulent fluctuations have a greater influence on the mean flow and on wake dynamics: the zone downstream of what would be the turbine tips ($z/D = \pm 0.5$), and downstream of the turbine hub. This is characteristic of regions of high velocity gradients, such as the outer region where the wake interacts with the faster moving ambient flow, and around the hub where velocity is zero. Pockets of high TKE coincide with the location of high principal Reynolds shear stress. Unfortunately, there are no turbulence measurements reported in the experimental tests to compare the resolved TKE and Reynolds shear stresses.

As described in the work carried out by Kang et al. [22], the pockets of high TKE and shear stress merge close to where turbine wake rotation diminishes. In our case this occurs around $5D$ downstream from the single device. In full-scale turbines, turbine blades and tips also generate turbulence and instabilities due to local flow effects of separation and instability, which are not present in our simulations due to the limitations of BEM. To address this issue, synthetic turbulence generation methods have been proposed, like the one used by Creech et. al [36] for wind turbines, and they could be considered in a further development of the methodology proposed in this study.

It is worth noting that on every plotted variable in Figures 7 and 8, the influence of the turbine can still be found up to $15D$ downstream of it, with mean longitudinal velocity still considerably reduced up to $20D$. Additionally, differences between the superior and inferior regions seen on the vertical planes shown above demonstrate an effect of the flume bed on wake development. The studied device occupies 60% of the water column, therefore bed effects can be considered important. This is evidenced in lower levels of TKE and shear stress in the inferior section of the wake, where the proximity to the boundary produces fluctuations of lower intensity, and create a vertical assymetry in the development of the wake.

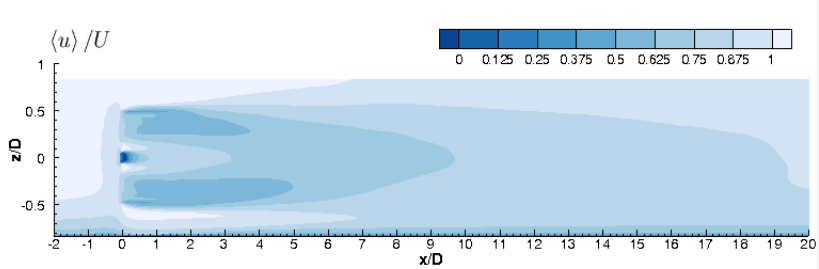

(a)

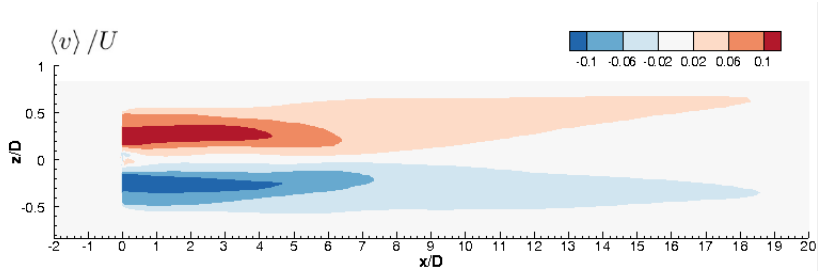

(b)

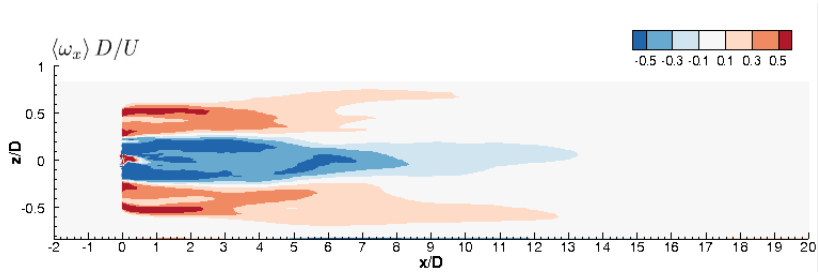

(c)

Figure 7: Contour plots of mean flow statistics at a vertical plane at y/D=0 for the single turbine case: (a) non-dimensional mean longitudinal velocity; (b) non-dimensional mean transverse velocity; (c) non-dimensional mean axial vorticity.

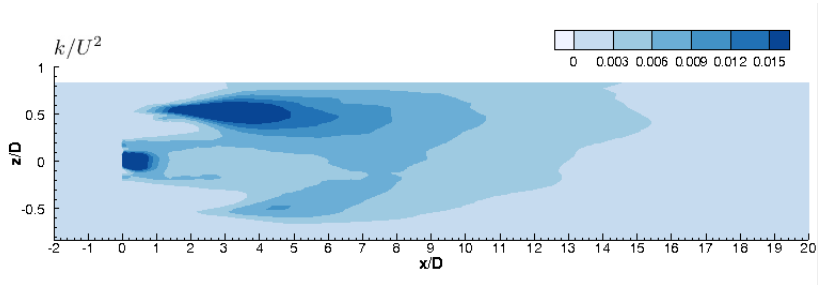

(a)

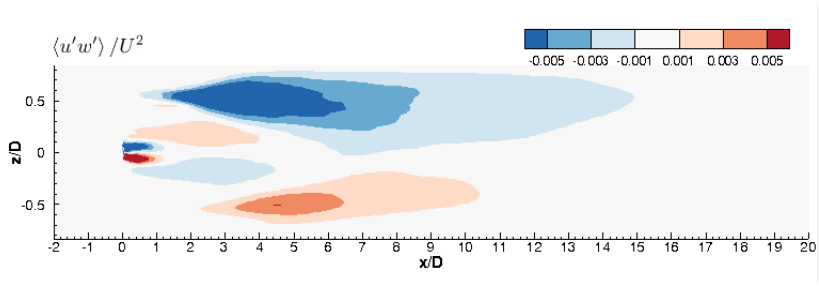

(b)

Figure 8: Contour plots of turbulence statistics at a vertical plane at y/D=0 for the single turbine case: (a) non-dimensional TKE; (b) non-dimensional principal Reynolds shear stress.

4.1.2. Instantaneous flow field

The q iso-surfaces shown in Figure 9 illustrate the effect our turbine model has on the instantaneous flow. First, even though BEM does not reproduce tip vortices, we still appreciate that the region surrounding our turbine is characterized by annular vortex shedding, in the length scale of the device diameter. Tip vortices and coherent structures that are generate downstream of the nacelle, interact as the wake develops affecting the turbulent intensity in the far wake. As detected also in wind turbines, these interactions are likely one of the factors responsible for the well-known wake meandering dynamics observed in three-blade turbines for different rotor diameters citep[e.g.][]ivanell2010stability,foti2018wake Second, the hub produces a rotating vortex whose size is in the scale of the hub diameter. Both structures gradually expand radially, and eventually interact, losing coherence at around $5D$. This is coincidental with the zones of increased turbulence statistics and decreased rotation in the wake.

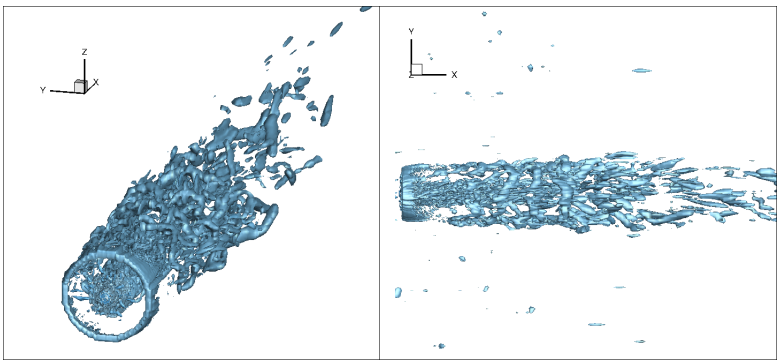

(a) (b)

Figure 9: Plots of instantaneous q iso-surfaces for the single turbine case. (a) three dimensional view; (b) plan view.

From the results presented above for the mean and instantaneous flow we can study the effects that a single turbine has on its surrounding environment, and how the wake develops downstream. They also show the validity of our BEM-DES implementation to represent tidal turbines. The instantaneous flow

field captures two counter-rotating regions downstream of the device. They interact around $5D$ downstream from the turbine, where rotation is considerably reduced and zones of high TKE and Reynolds stresses merge. These conditions are observed in the animations of q iso-surfaces, which show that the coherent structures are produced around the tip region of the turbine and around the hub. These structures lose their coherence in the same region where rotation decreases, and zones of high turbulence statistics interact.

This emphasizes the argument that even though BEM can be thought of as a simplified approach to represent tidal turbines, it can still provide fundamental insights into understanding wake hydrodynamics and the overall effect a device has on the ambient flow, both for the mean and the instantaneous flow field. As it will be discussed in the subsequent section, the approach remains specially beneficial when it is applied for arrays of multiple devices.

4.2. Flows past turbine arrays

4.2.1. Mean flow field

For the cases with ten turbines, we perform simulations of two rows of five devices in staggered and aligned configurations. Time-averaged comparisons of velocity deficit on a horizontal plane, and the evolution of the velocity in the streamwise direction are shown in Figures 10 and 11, respectively.

Figure 10 shows that the BEM-DES model gives better predictions compared to the experimental data than BEM-URANS simulations performed by Ingram & Olivieri [30], even though the latter approach included both turbine hub and nacelle geometry into the simulations. This improvement is seen in both doubled row cases, and confirmed using Mean Square Error and Nash-Sutcliffe Coefficient for comparison [52].

In Figure 11 we show the spatial evolution of the velocity U in the streamwise direction (x/D) for only the aligned case downstream of the second row of devices. The velocity U is measured at the hub height for the model and experimental results, and the different cross-stream positions (y/D) are identified by different colors. The symbols correspond to experimental observations, while

the lines represent the simulation results obtained from BEM-RANS (continuous lines) and our BEM-DES model (dashed lines). The results confirm the problems of the velocity profile with the BEM approach in the near field ($x/D < 2$), however, Figure 11 also shows that our BEM-DES model not only exhibits a better agreement in the far field, but the numerical results represent correctly the experimental data from $x/D \geq 4$, compared to the RANS simulations.

In general, the agreement of the model is improved by incorporating the new turbulence model, but at specific cross-stream positions, i.e. $y/D = 0$, BEM-RANS results can be closer to the experimental data.

These results underscore the importance of studying the effects of the turbulence model in capturing the dynamics of the wake, especially in the far-wake section, even with a more simplified geometrical representation of the devices. We can therefore conclude that the effects of the geometrical simplifications are dissipated by the large-scale coherent structures in the incoming flow from the upstream row and resolving with more detail the unsteady interactions of the wakes yields a better overall agreement of the mean velocity profiles, downstream of turbine arrays. This improvement was seen in both doubled row cases, and confirmed using Mean Square Error and Nash-Sutcliffe Coefficient for comparison [52]. Figure 11 depicts the region where the disagreement with experiments is worse is the immediate proximity of the device, $x/D < 2$, after which the profiles match the experimental predictions, except for $y/D = \pm 1.5$.

In addition, our simulations of turbine arrays showed that flow statistics vary considerably from the single turbine case when device wakes interact with each other and when turbines operate under the influence of upstream devices. As depicted in Figure 12 for the two staggered rows case, turbines in frontal rows have similar behavior as a single device, but this condition changes for downstream devices. In particular, as seen in Figure 12a, mean velocity deficit is higher downstream of posterior rows, and approximately $5D$ from the second row individual turbine wakes merge into a single array wake. One remarkable result is that rotation in the wake diminishes faster for posterior rows, like it is seen in Figures 12b and 12c. Rotation is considerably reduced around 3

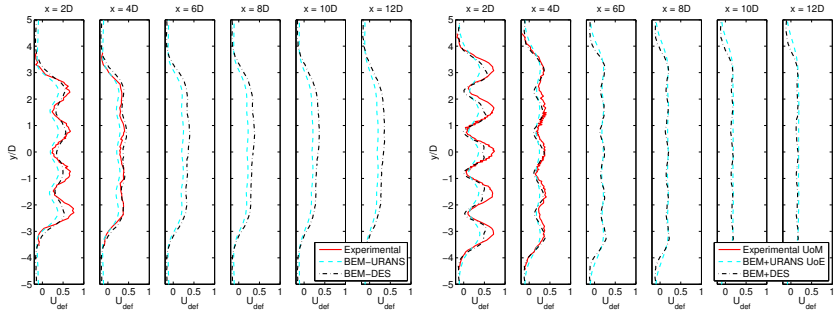

(a) (b)

Figure 10: Lateral profiles of mean velocity deficit, with distance measured from the second row of turbines. (a) two staggered rows; (b) two aligned rows. The BEM-DES simulations show good agreement with the experimental data even in the near wake region, with predictions being better that the BEM-URANS application.

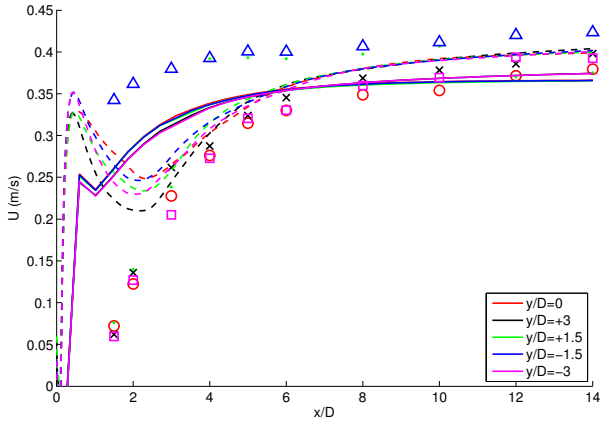

Figure 11: Axial profiles of mean longitudinal velocity downstream of the second row of the two aligned rows array, with velocity taken at hub height. Continuous lines represent BEM-URANS results, dashed lines are our BEM-DES results, and symbols represent experimental results, with different colors for different cross-stream positions (y/D). After $2D$ downstream the BEM-DES improves the representation on profile evolution, matching the experimental data.

diameters downstream of the devices, in contrast with the 5 diameters seen in the single turbine case. Arguably, the influence of upstream wakes contributes to destabilizing the wake of posterior devices faster, facilitating mixing between the wakes and the ambient flow, and accelerating wake development and recovery. These results were also seen for the aligned row case, with rotation diminishing near $x/D = 4$ downstream of the second row. Since both arrays have different longitudinal spacing between rows ($4D$ for the staggered case and $8D$ for the aligned one), downstream devices face upstream wakes at different stages of its development, with the aligned case at a distance large enough for the upstream wakes to have recovered more than in the staggered case. This changes the evolution of posterior wakes, but unfortunately our studied cases do not allow us to separate the effect of row alignment and longitudinal spacing on these results.

The distributions of TKE and Reynolds stress also illustrate the difference between single devices and arrays, and confirm that posterior wakes are characterized by higher influence of turbulent fluctuations on the mean flow. This is depicted in Figure 13 for the aligned rows. It can be seen that both turbulence statistics increase for downstream rows, evidencing strong interaction among turbine wakes, and also between wakes and the ambient flow. Second, we appreciate that the high turbulence zones at the outer wake and in the hub region merge closer to the turbines with respect with the single device study, in congruence with faster rotation reduction discussed above. Additionally, even though in the central part of the array turbulence statistics tend to diminish gradually and become neglible around $8D$ from the second row, they remain significant in the outer boundaries of the wake ($y/D = \pm 3.5$ in Figure 13), indicating that the ambient flow and the array wake keep interacting in this zone.

4.2.2. Instantaneous flow field

Figure 14 depicts the visualization of q iso-surfaces for both double row arrays, showing the presence of vortical structures. This clarifies the higher complexity of the flow faced by devices in posterior rows. Additionally, down-

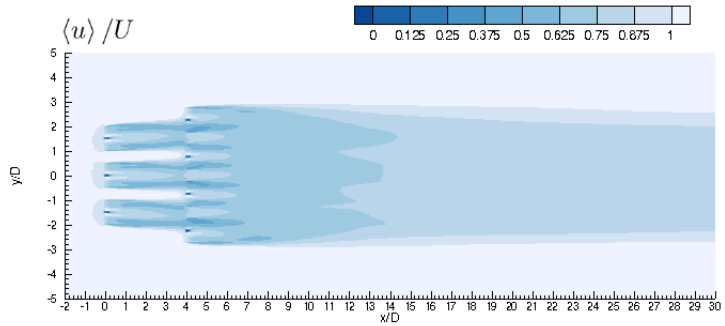

(a)

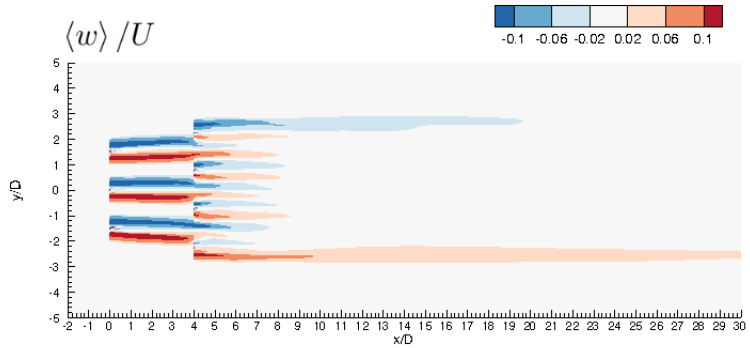

(b)

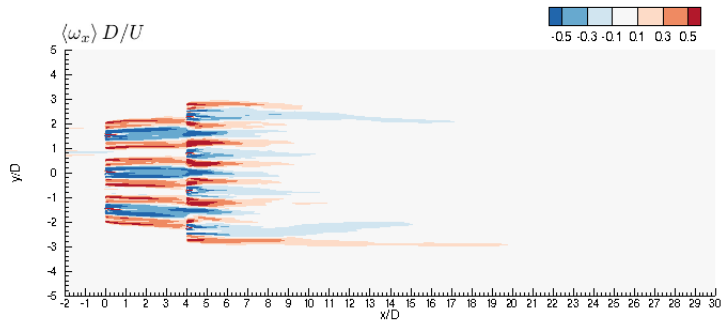

(c)

Figure 12: Contour plots of mean flow statistics at a horizontal plane at $z/D = 0$ for the two staggered rows case: (a) non-dimensional mean longitudinal velocity; (b) non-dimensional mean vertical velocity; (c) non-dimensional mean axial vorticity.

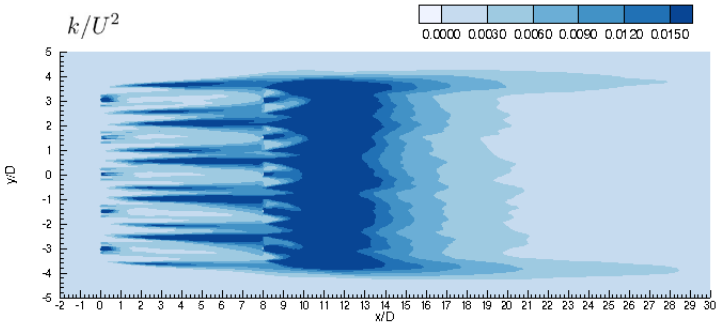

(a)

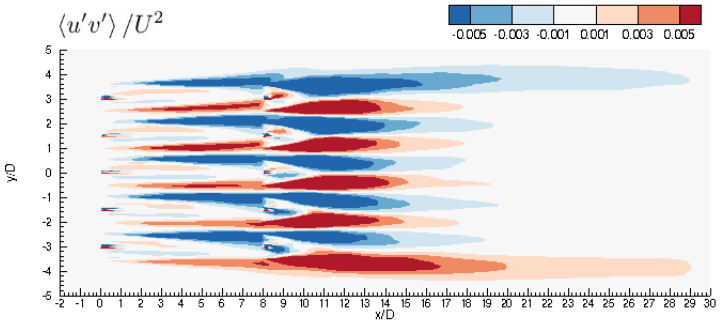

(b)

Figure 13: Contour plots of turbulence statistics at a vertical plane at y/D=0 for the single turbine case: (a) non-dimensional TKE; (b) non-dimensional principal Reynolds shear stress.

stream wakes have more complex structures, nevertheless, it is apparent from this Figure that vortical structures lose coherence faster than in the single device case, arguably because of the induced mixing of upstream wakes.

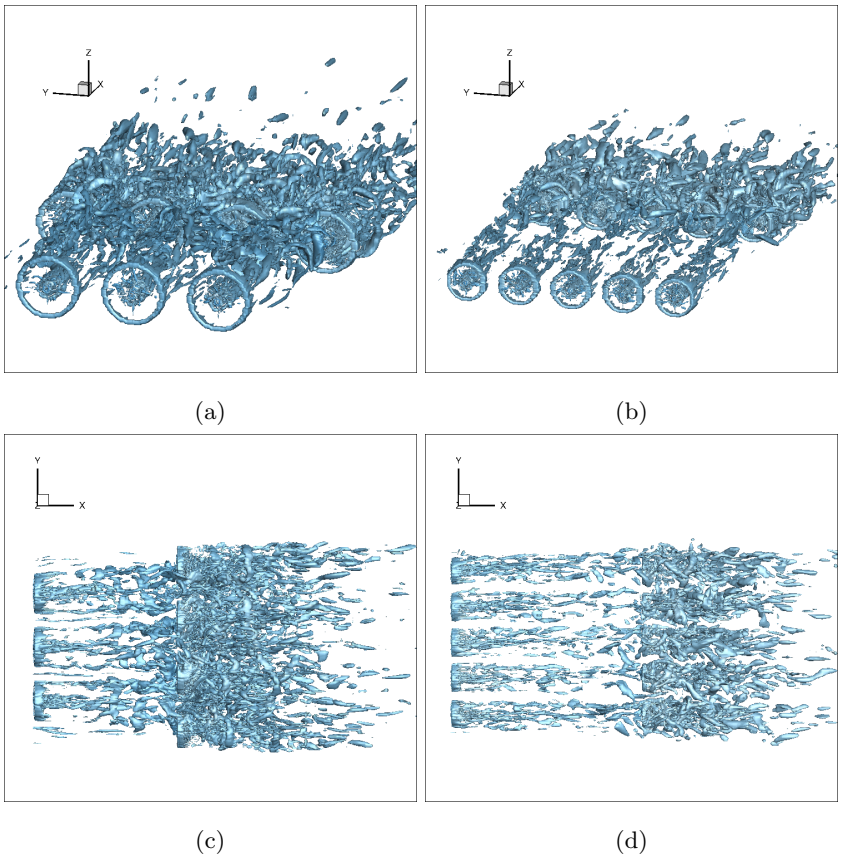

Figure 14: Instantaneous plots of q-isosurfaces for the studied arrays. (a),(c): two staggered rows; (b),(d): two aligned rows.

4.2.3. Effects on the bed

We compute the instantaneous friction or shear velocity u_* at each time step and on every point above the bed. The minimum value of u_* is zero when an instantaneous zero gradient condition produces no shear on the bed surface. The time series of u_* are used to compute the mean, standard deviation, and thus the coefficients of variation of the statistic.

For u_*, results show that regions of flow acceleration between turbines on the same row are characterized with higher levels of u_*, and therefore they are more likely to be affected by scour. On the contrary, downstream of the turbine centers, where velocity deficits are higher, u_* is smaller, and therefore they are zones that favor sediment deposition (see Figure 15a). These characteristics are in line with the experimental results obtained by Hill et. al [46, 47], who studied bedform evolution and sediment transport with an experimental scale device. It is worth noting that even though mean values for u_* are similar for frontal and posterior rows, temporal evolution is not. This is illustrated in Figure 15b, that shows how the RMS of u_* can be up to five times higher in the posterior row of the aligned rows array, with a deviation in the order of 10% of the mean value. Similar results where appreciated for the staggered rows case. As discussed previously, the region downstream of the second row of devices is characterized by an increase in TKE and Reynolds shear stress, with a flow with higher presence of vortices and turbulent fluctuations, which causes u_* to have larger temporal fluctuations of bed stresses in this zone too. This raises the question if designing tidal turbines considering mean values is sufficient, or if this temporal fluctuations are important enough to be considered in the device design and operation process.

4.2.4. Performance measurements

In order to grasp the bulk performance and power generation capability of tidal turbines it is common to use the power coefficient C_P as an indicator. As depicted in Figure 16, frontal devices showed results in the order of $C_P = 0.4$, in agreement of what was predicted by Stallard et. al [13] and Thomson et. al [29]. The mean values for the power coefficient decrease in 20% and 50% for the staggered and aligned rows cases, respectively. This is a consequence of downstream devices having to face a flow which has already been extracted of momentum by upstream devices, and that their longitudinal spacing is not enough for the wake to recover completely. From the figure it can also be clearly seen that increased velocity fluctuations associated with posterior rows have

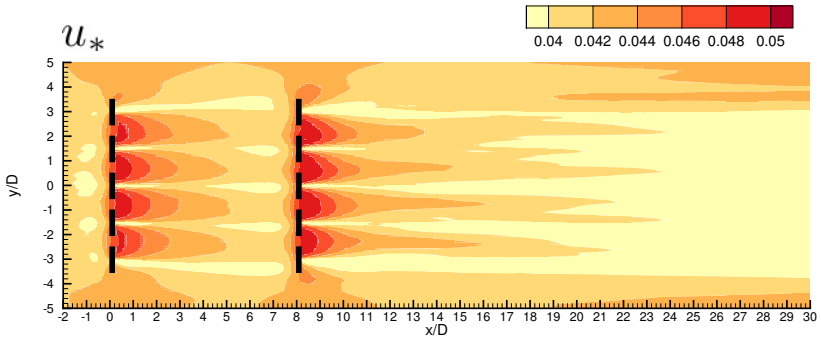

(a)

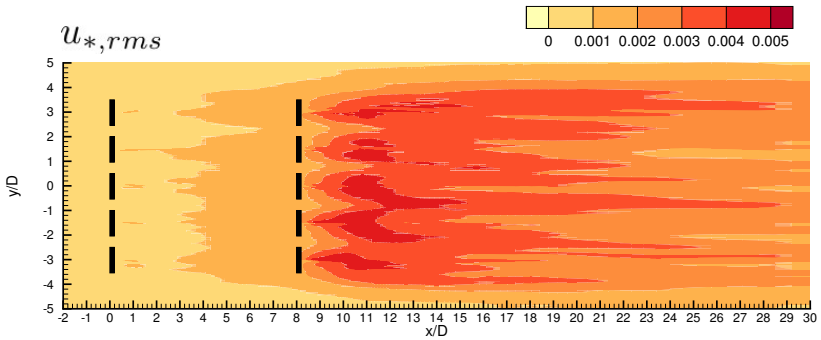

(b)

Figure 15: Contour plots of non-dimensionalized u_* and $u_{*,rms}$ for the ten turbine array: (a) time-averaged shear velocity, (b) shear velocity RMS.

consequences in the temporal evolution of power generation for these devices. For example, the standard deviation of C_P for posterior rows was almost four times higher than the frontal row for the staggered row cases, and almost twice as high for the aligned rows case. To further understand the temporal variability of this performance variable we calculated the Coefficient of Variation C_V, defined as the ratio between the standard deviation σ and mean value μ of a data series (i.e.: $C_V = \sigma/\mu$). On average, in the aligned rows case C_V was more than 8 times higher for posterior devices, and almost 3 times higher for the staggered rows case.

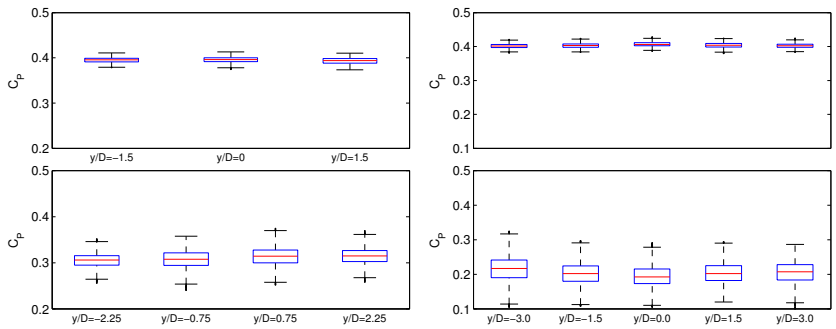

(a) (b)

Figure 16: Box plots for C_P. Each box plot is obtained with the timeseries of the respective turbine in the array. Superior plots are for frontal rows, and inferior for posterior ones. (a) two staggered rows; (b) two aligned rows.

Analyzing the coefficient of thrust C_T also gives an indication on overall turbine performance, specifically on the amount of thrust and loading a device will experience under its operation. Our results indicate the same type of behavior seen for C_P, frontal rows with good agreement to what was predicted experimentally, and posterior devices with lower values for the coefficient and considerably increased temporal variability, as seen in Figure 17. Posterior rows in the staggered array showed a 12% decrease in mean C_T, with a standard deviation and C_V, 3 and 4 times higher, respectively. In the aligned case, the mean values decreased in 20%, and had 2 and 3 times higher standard deviation

and C_V, respectively.

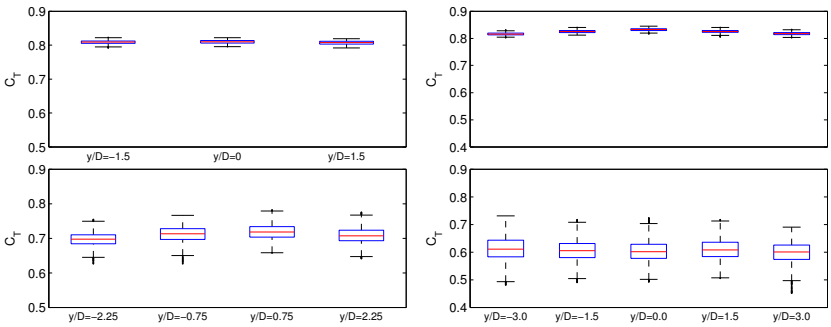

(a) (b)

Figure 17: Box plots for C_T. Each box plot is obtained with the timeseries of the respective turbine in the array. Superior plots are for frontal rows, and inferior for posterior ones. (a) two staggered rows; (b) two aligned rows.

It is interesting to note that the behavior when comparing with the BEM-URANS model is the same. As expected, the second row of turbines always has lower thrust and power coefficients than the frontal one. However, the difference between rows is greater in our model, as downstream devices report on average results with C_T 15% and C_P 10% lower than BEM-URANS from Ingram & Olivieri [30]. The greater flow complexity and unsteadiness captured when using a more advanced turbulence model, underscores the need to consider changes and to predict the variability of these coefficients, compared to using simpler turbulence approximations.

Comparing the studied arrays, temporal variability is higher and mean values are lower for the aligned rows case. Nevertheless, the scope of our study is not capable of isolating the effects of the alignment of rows and the streamwise spacing in the arrays, to understand the variables that dominate the wake flows. In future work we will perform a systematic study to control these variables, examining their influence on turbine performance and wake development.

From a turbine developer point of view the results discussed above are of critical importance, because they illustrate the fact that devices that interact

with other turbine wakes will have considerably higher unsteadiness in its power generation capacity and also on turbine loading. The first aspect is relevant also for the reliability of electricity generation, bearing in mind that fluctuations in power output increase the overall cost of this type of technology. In terms of loading, temporal fluctuations can be associated with material fatigue, and therefore must be considered when making design decisions both for single devices and for array configurations.

5. Conclusions and future work

The main objective of this study is to analyze the effects of HATTs on the surrounding environment, improving the understanding about how these MHK devices interact when they are placed in an array. Additionally, we intend to validate a new approach for studying arrays of multiple tidal turbines, hopefully encouraging its use for further applications. We couple a numerical model for the flow using a DES approach, based on our recent work [33, 32, 37], and a BEM tidal turbine representation based on the work carried out by Creech et al. [36]. To incorporate ambient turbulence we added a synthetic unsteady inlet [34, 35], to consider the effects of the upstream flow on the wake development. We apply the model to three different scenarios that were studied experimentally by Stallard et al. [13] and Thomson et al. [29], and numerically by Ingram and Olivieri [30] using a BEM-URANS model.

Even though our numerical methodology considers a simplified tidal turbine representation, and it does not capture every dynamic feature of the wakes near the turbines, we show that it provides fundamental insights on the dynamics of large tidal turbine arrays, whose demand on computational resources would be impractical if they were to be studied considering the exact geometry of the MHK devices together, with complex flow solvers such as DES or LES. The results show that by coupling a detailed flow solver like DES with a low-order turbine model as BEM we obtain fundamental information on turbine array characterization. The model gives predictions on variables such as mean

and instantaneous velocity fields, turbulence statistics, wake evolution, vortical structures on the flow, effects on the bed, and overall turbine performance measurements. Moreover, the model is capable of representing rotational features in the wake, which showed to dominate fundamental aspects of wake development and interactions. When comparing with a simpler turbulence model that had better geometrical representation of turbine hub and nacelle [30], our results improved the experimental predictions, while expanding the available information of the unsteadiness of the flow.

The comparison with the available experimental data shows that our model is capable of predicting the mean velocity distribution for every studied array. The region where larger differences were observed was in the near-wake region of turbines facing ambient flow (frontal rows and single devices), associated with our simplification of not considering the hub, nacelle, and support structure geometry in the simulations. However, this difference is not observed in the wake of turbines located at the downstream rows. Even in the near-wake region, the agreement with experiments was better than BEM-URANS with nacelle representation on average, as there are some discrepancies at some values of y/D. Arguably, large-scale structures produced by upstream devices dominate the evolution of the wake of downstream turbines, making geometrical simplifications and BEM limitations less relevant to predict mean velocity profiles. These results underscore the advantages of using a detailed flow solver such as DES, even when it is coupled with low-order models like BEM.

Studying a single turbine on a flume, the model shows that the device produces a streamwise velocity deficit that lasts up to $20D$ downstream. This deficit is accompanied by changes on the cross-stream velocity, vorticity, shear stresses, and increased TKE in the wake region. Rotation of the wake was seen to decrease considerably near $5D$ downstream from the device, accompanied in an increase in TKE and Reynolds stresses. Additionally, two vortex shedding regions were identified: (1) BEM produces an annular vortex with the scale of the device diameter instead of tip-vortices in the outer region of the device; and (2) Downstream of the turbine hub, a rotating vortex is produced. This

latter vortex widens radially and interacts with the outer vortex at a distance of around $5D$ downstream from the device, coinciding with the region of decreased rotation in the wake.

Regarding turbine arrays, we show that downstream rows face a more complex and dynamically-rich flow, with presence of vortices generated by the upstream MHK devices. Higher unsteadiness and the presence of upstream turbulent structures accelerate the merging of individual device wakes into a single array wake. This array wake is characterized by higher turbulence statistic levels, and the formation of large-scale vortical structures. When analyzing bed shear velocity, results indicated that the region between devices −where flow acceleration exists− is characterized by higher shear stresses, and therefore can be considered a zone where bed scour can occur. Conversely, in regions behind the turbines, stresses are low, and sediment deposition is more likely. In spite of the fact that mean values for u_* are similar for upstream and downstream rows, temporal fluctuations are up to five times higher in downstream rows, and owe up to a 10% variation from mean values. In terms of bulk turbine performance, we showed that coefficients C_T and C_P not only decrease significantly for turbines in downstream rows, but the have considerably more temporal variability. This issue can have important implications on turbine electricity generation capability, and on device material wear and fatigue.

Future developments of the model will include a more systematic approach for studying the effects of different array configurations, controlling variables such as streamwise and cross-stream spacing of the MHK devices. In addition, we will define the minimum resolution of the grid required to resolve the flow field, and optimize the computational cost when studying tidal turbines with this BEM-DES approach. In the current version, our model can easily incorporate new geometries for non-ducted turbines, so it can be used to analyze and compare new types of HATTs designs on various array deployments. It is also of interest to incorporate the ability to simulate ducted turbines, expanding the spectrum of HATT types that can be addressed by our model.

In the long-term, we aim at developing robust methodologies across temporal

and spatial scales to characterize potential sites, and analyze the impact of MHK devices. Therefore, we hope to use the model in conjunction with models of different scope, complexity, and scales, to gain further insight and opening new questions on the hydrodynamics feature associated with tidal energy generation.

Acknowledgements

We thank Mr. Jorge Sandoval and the comments provided by Dr. Angus Creech to this study. This work has been supported by Fondecyt project 1130940, by CONICYT grants 80160084 and 22160577, and by Chile's Marine Energy Research & Innovation Center (MERIC) CORFO project 14CEI2-28228. The study was partially supported by the RC UK Energy Programmes UK Centre for Marine Energy Research (EP/I027912/1). Powered@NLHPC: This research was partially supported by the supercomputing infrastructure of the NLHPC (ECM-02). We sincerely thank the Editor and two anonymous Reviewers who helped to improve the quality of the paper.

References

[1] O. Edenhofer, R. Pichs Madruga, Y. Sokona, Renewable Energy Sources and Climate Change Mitigation (Special Report of the Intergovernmental Panel on Climate Change), Vol. 6, 2012. doi:10.5860/CHOICE.49-6309.

[2] P. A. Lynn, Electricity From Wave and Tide: An Introduction to Marine Energy, 1st Edition, Wiley, Chichester, 2014.

[3] D. Magagna, A. Uihlein, Ocean energy development in Europe: Current status and future perspectives, International Journal of Marine Energy 11 (2015) 84–104. doi:10.1016/j.ijome.2015.05.001.

[4] M. I. Yuce, A. Muratoglu, Hydrokinetic energy conversion systems: A technology status review, Renewable and Sustainable Energy Reviews 14 (9) (2010) 2996–3004. doi:10.1016/j.rser.2010.06.016.

[5] M. Khan, G. Bhuyan, M. Iqbal, J. Quaicoe, Hydrokinetic energy conversion systems and assessment of horizontal and vertical axis turbines for river and tidal applications: A technology status review, Applied Energy 86 (10) (2009) 1823–1835. doi:10.1016/j.apenergy.2009.02.017.

[6] M. Melikoglu, Current status and future of ocean energy sources: A global review, Ocean Eng. 148 (2018) 563–573.

[7] A. Uihlein, D. Magagna, Wave and tidal current energy - A review of the current state of research beyond technology, Renewable and Sustainable Energy Reviews 58 (2016) 1070–1081. doi:10.1016/j.rser.2015.12.284.

[8] B. Polagye, B. V. Cleve, K. Kirkendall, A. Copping, Environmental effects of tidal energy development, in: Proceedings of a Scientific Workshop, 2010.

[9] I. G. Bryden, S. J. Couch, ME1 - Marine energy extraction: Tidal resource analysis, Renewable Energy 31 (2) (2006) 133–139. doi:10.1016/j.renene.2005.08.012.

[10] L. P. Chamorro, C. Hill, S. Morton, C. Ellis, R. E. A. Arndt, F. Sotiropoulos, On the interaction between a turbulent open channel flow and an axial-flow turbine, Journal of Fluid Mechanics 716 (2013) 658–670. doi:10.1017/jfm.2012.571.

[11] P. Mycek, B. Gaurier, G. Germain, G. Pinon, E. Rivoalen, Experimental study of the turbulence intensity effects on marine current turbines behaviour. Part I: One single turbine, Renewable Energy 66 (2014) 729–746. doi:10.1016/j.renene.2013.12.036.

[12] P. Mycek, B. Gaurier, G. Germain, G. Pinon, E. Rivoalen, Experimental study of the turbulence intensity effects on marine current turbines behaviour. Part II: Two interacting turbines, Renewable Energy 68 (2014) 876–892. doi:10.1016/j.renene.2013.12.048.

[13] T. Stallard, R. Collings, T. Feng, J. Whelan, Interactions between tidal turbine wakes: Experimental study of a group of three-bladed rotors, Philosophical Transactions of the Royal Society A 371 (1985) (2013) 1471–2962.

[14] V. T. Nguyen, S. S. Guillou, J. Thiebot, A. S. Cruz, Modelling turbulence with an Actuator Disk representing a tidal turbine, Renewable Energy 97 (2016) 625–635. doi:10.1016/j.renene.2016.06.014.

[15] W. M. J. Batten, M. E. Harrison, A. Bahaj, Accuracy of the actuator disc-RANS approach for predicting the performance and wake of tidal turbines, Philosophical transactions. Series A, Mathematical, physical, and engineering sciences 371 (1985) (2013) 20120293. doi:10.1098/rsta.2012.0293.

[16] T. Blackmore, W. M. J. Batten, A. Bahaj, Influence of turbulence on the wake of a marine current turbine simulator, Proc. R. Soc. A 470 (20140331) (2014) 1–17. doi:10.1098/rspa.2014.0331.

[17] A. Creech, A. Borthwick, D. Ingram, Effects of Support Structures in an LES Actuator Line Model of a Tidal Turbine with Contra-rotating Rotors, Energies 10 (726) (2017) 1–25. doi:10.20944/preprints201703.0230.v1.

[18] I. Afgan, J. McNaughton, S. Rolfo, D. D. Apsley, T. Stallard, P. Stansby, Turbulent flow and loading on a tidal stream turbine by LES and RANS, International Journal of Heat and Fluid Flow 43 (2013) 96–108. doi:10.1016/j.ijheatfluidflow.2013.03.010.

[19] T. P. Lloyd, S. R. Turnock, V. F. Humphrey, Assessing the influence of inflow turbulence on noise and performance of a tidal turbine using large eddy simulations, Renewable Energy 71 (2014) 742–754. doi:10.1016/j.renene.2014.06.011.

[20] M. Churchfield, Y. Li, P. Moriarty, A large-eddy simulation study of wake propagation and power production in an array of tidal-current turbines., Philosophical transactions. Series A, Mathematical, physical, and engineering sciences 371 (1985) (2013) 20120421. doi:10.1098/rsta.2012.0421.

[21] G. Pinon, P. Mycek, G. Germain, E. Rivoalen, Numerical simulation of the wake of marine current turbines with a particle method, Renewable Energy 46 (2012) 111–126. doi:10.1016/j.renene.2012.03.037.

[22] S. Kang, X. L. Yang, F. Sotiropoulos, On the onset of wake meandering for an axial flow turbine in a turbulent open channel flow, Journal of Fluid Mechanics 744 (2014) (2014) 376–403. doi:Doi10.1017/Jfm.2014.82.

[23] S. Chawdhary, C. Hill, X. Yang, M. Guala, D. Corren, J. Colby, F. Sotiropoulos, Wake characteristics of a TriFrame of axial-flow hydrokinetic turbines, Renewable Energydoi:10.1016/j.renene.2017.03.029.

[24] I. Masters, J. C. Chapman, M. R. Willis, J. A. C. Orme, A robust blade element momentum theory model for tidal stream turbines including tip and hub loss corrections, Journal of Marine Engineering and Technology 10 (1). doi:10.1080/20464177.2011.11020241.

[25] M. Edmunds, A. J. Williams, I. Masters, T. N. Croft, An enhanced disk averaged CFD model for the simulation of horizontal axis tidal turbines, Renewable Energy 101 (2017) 67–81. doi:10.1016/j.renene.2016.08.007.

[26] I. Masters, R. Malki, A. J. Williams, T. N. Croft, The influence of flow acceleration on tidal stream turbine wake dynamics: A numerical study using a coupled BEM-CFD model, Applied Mathematical Modelling 37 (16-17) (2013) 7905–7918. doi:10.1016/j.apm.2013.06.004.

[27] P. R. Spalart, Detached-Eddy Simulation, Annual Review of Fluid Mechanics 41 (1) (2009) 181–202. doi:10.1146/annurev.fluid.010908.165130.

[28] CCP-WSI Focus Group, Wave Structure Interaction Computation and Experiment Roadmap. Part 1: A Report on the 1st CCP-WSI Focus Group Workshop, Tech. Rep. September, Plymouth University (2016).

[29] M. Thomson, R. Collings, T. Stallard, Array Scale Experimental Test Report. PerAWaT Deliverable MA1003 WG4 WP2 D5, Tech. rep., Energy Technologies Institute, Manchester (2011).

[30] D. Ingram, D. A. Olivieri, Tidal array scale numerical modelling. Interactions within a farm (Steady Flow). PerAWaT MA1003 Deliverable WG3 WP2 D5a, Tech. rep., Energy Technologies Institute, Edinburgh (2012).

[31] P. R. Spalart, W.-H. Jou, M. Strelets, S. R. Allmaras, Comments on the feasibility of LES for wings, and on a hybrid RANS/LES approach., in: C. Liu, Z. Liu (Eds.), Advances in DNS/LES, Greyden Press, Ruston, 1997, pp. 138–147.

[32] C. Escauriaza, F. Sotiropoulos, Lagrangian model of bed-load transport in turbulent junction flows, Journal of Fluid Mechanics 666 (2011) 36–76. doi:Doi10.1017/S0022112010004192.

[33] J. Paik, C. Escauriaza, F. Sotiropoulos, Coherent structure dynamics in turbulent flows past in-stream structures: Some insights gained via numerical simulation, Journal of Hydraulic Engineering 136 (12) (2010) 981–993. doi:doi:10.1061/(ASCE)HY.1943-7900.0000089.

[34] R. Laraufie, S. Deck, Assessment of reynolds stresses tensor reconstruction methods for synthetic turbulent inflow conditions. application to hybrid rans/les methods, International Journal of Heat and Fluid Flow 42 (2013) 68 – 78. doi:http://dx.doi.org/10.1016/j.ijheatfluidflow.2013.04.007.

[35] A. Smirnov, S. Shi, I. Celik, Random Flow Generation Technique for Large Eddy Simulations and Particle-Dynamics Modeling, Journal of Fluids Engineering 123 (2) (2001) 359. doi:10.1115/1.1369598.

[36] A. Creech, W. G. Früh, A. E. Maguire, Simulations of an Offshore Wind Farm Using Large-Eddy Simulation and a Torque-Controlled Actuator Disc

Model, Surveys in Geophysics 36 (3) (2015) 427–481. arXiv:1410.3650, doi:10.1007/s10712-015-9313-7.

[37] C. Escauriaza, F. Sotiropoulos, Initial stages of erosion and bed form development in a turbulent flow around a cylindrical pier, Journal of Geophysical Research: Earth Surface 116 (F3), f03007. doi:10.1029/2010JF001749. URL http://dx.doi.org/10.1029/2010JF001749

[38] P. R. Spalart, S. R. Allmaras, A one-equation turbulence model for aerodynamic flows, La Recherche Aérospatiale 1 (1994) 5–21.

[39] J. Paik, C. Escauriaza, F. Sotiropoulos, On the bimodal dynamics of the turbulent horseshoe vortex system in a wing-body junction, Physics of Fluids 19 (2007) 045107.

[40] O. Link, C. González, M. Maldonado, C. Escauriaza, Coherent structure dynamics and sediment particle motion around a cylindrical pier in developing scour holes, Acta Geophysica 60 (2012) 1689–1719.

[41] R. Malki, I. Masters, A. J. Williams, T. N. Croft, The variation in wake structure of a tidal stream turbine with flow velocity, in: L. Eca, E. Oñate, J. García-Espinosa, T. Kvamsdal, P. Bergan (Eds.), Computational Methods in Applied Sciences, Vol. 29, Springer Science + Business Media, Dordretch, 2013, pp. 137–148. doi:10.1007/978-94-007-6143-8_8.

[42] B. Elie, G. Oger, P.-E. Guillerm, B. Alessandrini, Simulation of horizontal axis tidal turbine wakes using a weakly-compressible cartesian hydrodynamic solver with local mesh refinement, Renewable Energy 108 (2017) 336–354.

[43] F. Maganga, G. Germain, J. King, G. Pinon, E. Rivoalen, Experimental study to determine flow characteristic effects on marine current turbine behaviour, 8th European Wave and Tidal Energy Conference 4 (May) (2009) 661–667. doi:http://dx.doi.org/10.1049/iet-rpg.2009.0205.

[44] G. R. Tabor, M. H. Baba-Ahmadi, Inlet conditions for large eddy simulation: A review, Computers and Fluids 39 (4) (2010) 553–567. doi:10.1016/j.compfluid.2009.10.007.

[45] J. C. R. Hunt, a. a. Wray, P. Moin, Eddies, streams, and convergence zones in turbulent flows, Center for Turbulence Research, Proceedings of the Summer Program (1970) (1988) 193–208. doi:CTR-S88.

[46] C. Hill, M. Musa, L. P. Chamorro, C. Ellis, M. Guala, Local Scour around a Model Hydrokinetic Turbine in an Erodible Channel, Journal of Hydraulic Engineering 140 (8) (2014) 0414037. doi:10.1061/(ASCE)HY.1943-7900.0000900.

[47] C. Hill, M. Musa, M. Guala, Interaction between instream axial flow hydrokinetic turbines and uni-directional flow bedforms, Renewable Energy 86 (2016) 409–421. doi:10.1016/j.renene.2015.08.019.

[48] G. Kalitzin, G. Medic, G. Iaccarino, P. Durbin, Near-wall behavior of RANS turbulence models and implications for wall functions, Journal of Computational Physics 204 (1) (2005) 265–291. doi:10.1016/j.jcp.2004.10.018.

[49] J. Riglin, W. Chris Schleicher, I. H. Liu, A. Oztekin, Characterization of a micro-hydrokinetic turbine in close proximity to the free surface, Ocean Engineering 110 (2015) 270–280. doi:10.1016/j.oceaneng.2015.10.026.

[50] I. Masters, A. J. Williams, T. Croft, M. Togneri, M. Edmunds, E. Zangiabadi, I. Fairley, H. Karunarathna, A Comparison of Numerical Modelling Techniques for Tidal Stream Turbine Analysis, Energies 8 (2015) 7833–7853. doi:10.3390/en8087833.

[51] A. Creech, W.-G. Früh, Modelling wind turbine wakes for wind farms, in: J. Lehr (Ed.), Alternative Energy and Shale Gas Encyclopedia, 2016, Ch. 4. doi:10.1002/9781119066354.ch.4.

[52] N. D. Bennett, B. F. W. Croke, G. Guariso, J. H. A. Guillaume, S. H. Hamilton, A. J. Jakeman, S. Marsili-Libelli, L. T. H. Newham, J. P.

Norton, C. Perrin, S. A. Pierce, B. Robson, R. Seppelt, A. A. Voinov, B. D. Fath, V. Andreassian, Characterising performance of environmental models, Environmental Modelling and Software 40 (2013) 1–20. doi: 10.1016/j.envsoft.2012.09.011.